

Prospects for the Determination of H_0 through Observation of Multiply Imaged Supernovae in Galaxy Cluster Fields

Adam S. Bolton and Scott Burles

*Department of Physics and Center for Space Research
 Massachusetts Institute of Technology
 77 Massachusetts Avenue, Cambridge, MA 02139*

bolton@mit.edu, burles@mit.edu

ABSTRACT

We assess the possibility of determining the Hubble constant H_0 by measuring time delays between multiple images of supernovae gravitationally lensed by rich clusters of galaxies and combining these delay measurements with detailed cluster-potential models based on other lensing constraints. Such a lensing determination of H_0 would be complementary to those obtained from galaxy-QSO lensing studies, and could potentially be better calibrated. We show that relatively low-redshift ($z \sim 0.2$), significantly elliptical clusters have appreciable lensing cross sections for observable image pairings with tractable time delays on the order of a few years despite large lensing mass scales. We find that a targeted search for such image pairs would be a significant undertaking for current observatories, but that it would be appropriate for a facility such as the proposed Large-aperture Synoptic Survey Telescope.

Subject headings: distance scale—gravitational lensing—galaxies: clusters: general—supernovae: general

1. Introduction

The best measurements of the Hubble constant (H_0) based on the Cepheid-calibrated distance ladder and on the cosmic microwave background agree impressively with one another: $H_0 = 72 \pm 8 \text{ km s}^{-1} \text{ Mpc}^{-1}$ and $H_0 = 72 \pm 5 \text{ km s}^{-1} \text{ Mpc}^{-1}$, respectively (Freedman et al. 2001; Spergel et al. 2003). However, these values are inconsistent with much lower values of H_0 based upon measurements of gravitational lens time delays and the assumption that lensing galaxies have extended dark halos (Kochanek 2002a,b, 2003). In this paper we

explore the possibility of determining H_0 by monitoring known strong-lensing galaxy clusters and measuring time delays between multiple images of high-redshift supernovae (SNe).

The number of known giant-arc clusters is encouraging. Wu et al. (1998) present a summary of 38 strongly lensing clusters from the literature, containing a total of 48 giant arcs and arclets (see also Williams, Navarro, & Bartelmann (1999)). More recently, Luppino et al. (1999) have reported the discovery of 8 more giant-arc clusters, Gladders, Yee, & Ellingson (2002) 6 more, and Zaritsky & Gonzalez (2003) 3 more. Recent observations of the galaxy cluster Abell 1689 with the Advanced Camera for Surveys (ACS) on the *Hubble Space Telescope* have revealed at least 30 new multiply-imaged background sources, with an average of ~ 3 images each (D. Coe, 9 January 2003 presentation “Deep ACS and Keck Observations of A1689”, in conference “Gravitational Lensing: a Unique Tool for Cosmology”, Aussois, Savoie, France). All these image systems (together with previously known strongly lensed features) provide constraints on the projected gravitational potential of the cluster—many more constraints than a quadruple-image quasar lens system places on its lensing galaxy. In addition, since multiple strongly lensed sources behind a single galaxy cluster in general lie at different redshifts, the cluster potential map will not suffer the “mass sheet degeneracy” that afflicts galaxy-quasar lens systems (Saha 2000). Although A1689 is perhaps the strongest cluster lens in the sky, we may assume that other known strong-lensing clusters will likewise exhibit many new multiple-image systems when observed with ACS and later instruments, and detailed cluster modeling like that of AbdelSalam, Saha, & Williams (1998a,b) and Kneib et al. (1995, 1996) but with increased accuracy will become possible. Thus although the structure of galaxy clusters is in general more complex than that of individual galaxies, the projected potentials of clusters may in the near future be more tightly constrained by lensing than those of individual galaxies, and cluster-lens time delay would therefore be more precisely calibrated. (See Schechter (2000) for a general discussion of the determination of H_0 from gravitational-lens time delays.)

This work is distinguished from previous studies by its quantitative focus on the possibility of measuring SN-image time delays in cluster-scale lens systems, and combining them with additional strong-lensing constraints to determine H_0 . The original proposition to measure H_0 using gravitational lens time delays envisioned distant supernovae (SNe) as the variable sources to be lensed by intervening galaxies (Refsdal 1964); quasars and their variability had yet to be discovered. Kovner & Paczyński (1988) examined the possibility of observing SNe exploding within giant-arc source galaxies. They made a detailed analysis for a SN very near to and inside a caustic “cusp” and showed that for such configurations the time delay between multiple images could be as short as days to weeks, although they did not explicitly consider the possibility of making an H_0 determination. Giraud (1992) reported the detection of variability in two separate arclets of the cluster Cl 0302+1658,

consistent with a single source and a time delay of 1 to 2 years. Various papers have examined magnification and time delay effects for SNe in field surveys lensed by intervening halos across a spectrum of mass scales (Linder, Schneider, & Wagoner 1988; Marri & Ferrara 1998; Dahlén & Fransson 1999; Marri, Ferrara, & Pozetti 2000; Porciani & Madau 2000; Holz 2001; Goobar et al. 2002; Oguri, Suto, & Turner 2003; Oguri & Kawano 2003), and several have explicitly considered the possibility of constraining H_0 using SN time delays. However, all these works have modeled the lenses as circular, and in this paper we show that circular models seriously under-predict the capacity for cluster-scale lenses to produce multiple images with reasonably short time delays (as one might anticipate based on the results of Kovner & Paczyński (1988) for sources very near to the caustic cusp of a lens). Other studies have considered targeted searches for lensed SNe in galaxy cluster fields (Miralda-Escudé & Rees 1997; Kolatt & Bartelmann 1998; Saini, Raychaudhury, & Shchekinov 2000; Sullivan et al. 2000; Gal-Yam, Maoz, & Sharon 2002; Gunnarsson & Goobar 2002), but their quantitative focus has been on pure SN detection rates and not on the prospects for measuring time delays that we quantify here. With the exception of Saini et al. (2000), these works have also approximated clusters with circularly symmetric lens models.

This paper is organized as follows. Section 2 presents a brief discussion of relevant gravitational lens theory and defines the particular lensing cross section that is central to our calculations. In Section 3, we examine the lensing behavior of several cluster models in the context of observational constraints on minimum magnification and maximum time delay. Section 4 discusses the accuracy in the determination of H_0 that we might hope to obtain from individual cluster time delays, both for a simplified model and for realistic models. Section 5 presents a calculation of detection rates for observable SN image pairings with acceptable time delays in the strong-lensing region of a specific cluster. Our approach in this section is similar to that of Sullivan et al. (2000) and Gunnarsson & Goobar (2002) (and differs from that of Saini et al. (2000)) in that we do not directly consider the possibility of SNe within known lensed galaxies, but rather attempt a prediction of SN detection rates in a targeted cluster field based on an assumed cluster mass model and cosmic supernova rate density function. (Lanzetta et al. (2002) argue that above redshifts of ~ 1.5 –2, even the Hubble Deep Field observations are insensitive to the surface brightness of most rest-frame ultraviolet emission.) Finally, in Section 6 we discuss the observational outlook in view of the calculations of Section 5. We find that a measurement of H_0 based on cluster time delays would be challenging but not impossible with today’s telescopes and instruments, and that it would be an appropriate project for a large telescope operating in a dedicated survey mode such as the proposed Large-aperture Synoptic Survey Telescope (*LSST*) (Tyson et al. 2002).

Throughout this paper, we assume a flat, vacuum-dominated cold dark matter (Λ CDM) cosmology with matter and vacuum density parameters $\Omega_M = 0.3$, $\Omega_\Lambda = 0.7$. For the Hubble constant, we take $H_0 = 70 h_{70} \text{ km s}^{-1} \text{ Mpc}^{-1}$ with $h_{70} = 1$.

2. Lensing Theory

Gravitational lensing can be described elegantly through the application of Fermat’s principle (Schneider 1985; Blandford & Narayan 1986). For a source at (2-vector) angular position $\vec{\beta}$, the time of arrival relative to the unlensed case for image positions $\vec{\theta}$ is given by

$$t = \frac{(1+z_L)}{c} \frac{D_L D_S}{D_{LS}} \left[\frac{1}{2} (\vec{\theta} - \vec{\beta})^2 - \psi(\vec{\theta}) \right] , \quad (1)$$

where z_L is the lens redshift, D_L , D_S , and D_{LS} are angular diameter distances to the lens, to the source, and from the lens to the source, and $\psi(\vec{\theta})$ is proportional to the Newtonian potential of the lens projected perpendicular to the line of sight (Narayan & Bartelmann 1996). Images of the source will be seen at positions $\vec{\theta}$ where the arrival time is stationary: that is, at solutions to the “lens equation” obtained by setting the gradient with respect to $\vec{\theta}$ of (1) to zero:

$$\vec{\beta}(\vec{\theta}) = \vec{\theta} - \vec{\nabla}_{\vec{\theta}} \psi(\vec{\theta}) . \quad (2)$$

The scalar magnification μ (the flux ratio of lensed to unlensed images of a source) is given by the ratio of lensed to unlensed differential angular area, thus it is given by the Jacobian determinant of the mapping $\vec{\theta}(\vec{\beta})$ (the local inverse of (2)):

$$\mu = \det \left(\frac{d\theta_i}{d\beta_j} \right) = \left[\det \left(\frac{d\beta_j}{d\theta_i} \right) \right]^{-1} . \quad (3)$$

For an excellent presentation of gravitational lensing in more detail, we recommend the work of Narayan & Bartelmann (1996).

The detection of multiply imaged SNe will be limited by both attainable photometric depth and maximum tolerable time delay. Accordingly, we define $\sigma(\mu_{\min}, \Delta t_{\max})$ to be the angular cross section in the source plane for lensing into a pair of images with the fainter of the two having (absolute-value) magnification of at least μ_{\min} and the time delay between the two being at most Δt_{\max} . For a particular physical lens model, this cross section will depend upon the redshifts of the lens and the source, but we will suppress this dependence in our notation.

3. Lens Models

In this section we examine $\sigma(\mu_{\min}, \Delta t_{\max})$ for three progressively more detailed lens models, and discuss the issue of normalization for the purpose of comparing between them. These models have been analyzed in detail by Kassiola & Kovner (1993) and by Kormann,

Schneider, and Bartelmann (1994). Particularly convenient formulas are given by Keeton & Kochanek (1998). We refer the reader to these papers for analytic lensing potential expressions and for detailed discussions of the models’ lensing behavior. Wherever numerical solution of the lens equation (2) is needed, we use our own implementation of the grid-based numerical lens-equation solution algorithm with 2D Newton-method solution refinement described by Schneider, Ehlers, & Falco (1992).

3.1. Singular Isothermal Sphere

The simplest reasonable model for an extended astrophysical mass distribution is the familiar singular isothermal sphere (SIS). It is parametrized solely by its velocity dispersion σ_v . The scaled, projected mass distribution (convergence) of the SIS is given by

$$\kappa = \frac{\Sigma}{\Sigma_{\text{cr}}} = \frac{1}{2} \frac{\theta_E}{|\vec{\theta}|} = \frac{1}{2} \frac{\theta_E}{\sqrt{\theta_x^2 + \theta_y^2}} . \quad (4)$$

Here, Σ is the physical surface mass density of the lens and $\Sigma_{\text{cr}} = (c^2/4\pi G)(D_S/D_L D_{LS})$ is the so-called critical surface mass density. θ_E is the “Einstein radius” that sets the sole angular scale of the model for given lens and source redshifts:

$$\theta_E = 4\pi \frac{\sigma_v^2}{c^2} \frac{D_{LS}}{D_S} \text{ (radians)} = (28.8 \text{ arcsec}) \left(\frac{\sigma_v}{1000 \text{ km/s}} \right)^2 \frac{D_{LS}}{D_S} . \quad (5)$$

The lensing potential of the SIS is simply $\psi(\vec{\theta}) = \theta_E |\vec{\theta}|$.

We can obtain $\sigma(\mu_{\text{min}}, \Delta t_{\text{max}})$ for the SIS analytically. If the angular distance β from the source (i.e., SN) position to the lens center is less than θ_E , two images will be observed along a line on the sky through the source position and the lens center: one at a distance $\theta_E + \beta$ from the lens center (in the direction of the source) with magnification $1 + \theta_E/\beta$ and one at a distance $\theta_E - \beta$ (in the direction opposite the source) with magnification $1 - \theta_E/\beta$ (Narayan & Bartelmann 1996, for example). This second, fainter image corresponds to a saddle point of the arrival time function (1); its negative magnification signals a reversal of image parity. It is this magnification that determines the μ_{min} dependence of $\sigma(\mu_{\text{min}}, \Delta t_{\text{max}})$ as defined. If we substitute the solutions $\theta_E \pm \beta$ into (1) (taking into account vectorial considerations) and form the difference, we find that the time delay between the two images is

$$\Delta t = \frac{2(1 + z_L)}{c} \frac{D_L D_S}{D_{LS}} \theta_E \beta \equiv 2\tau \frac{\beta}{\theta_E} , \quad (6)$$

where we have defined a characteristic lensing timescale by τ as implied. For a cluster velocity dispersion $\sigma_v = 1000 \text{ km/s}$, τ increases steeply at first with increasing source redshift, then

levels off around $\sim 25 h_{70}^{-1}$ years for $z_L = 0.1$ or $\sim 70\text{--}80 h_{70}^{-1}$ years for $z_L = 0.4$. (In Section 3.2 we will relieve our sense of discouragement over such long timescales.)

We see that for the SIS a given β corresponds to a unique Δt as given by (6) and a unique (absolute-value) magnification of $\theta_E/\beta - 1$ for the fainter image, so the form of $\sigma(\mu_{\min}, \Delta t_{\max})$ is particularly simple: we have two singly limited cross sections given by

$$\sigma(\mu_{\min}) = \pi\theta_E^2(\mu_{\min} + 1)^{-2} \quad (7a)$$

$$\sigma(\Delta t_{\max}) = \frac{1}{4}\pi\theta_E^2(\Delta t_{\max}/\tau)^2, \quad (7b)$$

and

$$\sigma(\mu_{\min}, \Delta t_{\max}) = \min[\sigma(\mu_{\min}), \sigma(\Delta t_{\max})]. \quad (8)$$

That is, for a given $(\mu_{\min}, \Delta t_{\max})$, we are either magnification-limited or delay-limited. (Arguably the maximum possible double-image cross section $\pi\theta_E^2$ should be enforced in (7b), but it is built into (7a) and thereby propagates to (8).)

3.2. Singular Isothermal Ellipsoid

By making the isodensity contours of the SIS elliptical with a minor-to-major axis ratio q , we get the singular isothermal ellipsoid (SIE) model:

$$\kappa = \frac{1}{2} \frac{\theta_E}{\sqrt{q\theta_x^2 + q^{-1}\theta_y^2}}. \quad (9)$$

As noted by Kormann et al. (1994), the total mass enclosed within a given isodensity contour remains constant with changing q at fixed θ_E when κ is expressed in this form. We adopt this normalization as a basis for comparing models of differing axis ratios, with θ_E still given as a function of σ_v and source and lens redshifts by (5).

The introduction of ellipticity leads to richer lensing phenomena. Most significantly, we acquire a cross section for quadruple imaging. For axis ratios q less than 1 but greater than about 0.394, four images of a source will form if the source position lies within a diamond-shaped “tangential” caustic surrounding the lens center and inside the original border between singly and doubly imaged regions (the “radial cut”). Labeling these quad images in order of increasing arrival time, 1 and 2 are minima of the arrival time function and 3 and 4 are saddle points. 2 and 3 are in general of much greater absolute magnification than 1 and 4. We now have the possibility of three independent image pairings. For $q < \approx 0.394$, the major-axis cusps of the tangential caustic extend outside the radial cut and are referred

to as “naked cusps”; sources within the cusps but outside the radial cut will be triply imaged. Kassiola & Kovner (1993) Figure 1(d,e) illustrates naked and non-naked cusps.

The SIE model has an angular scale invariance that allows us to generate the function $\sigma(\mu_{\min}, \Delta t_{\max})$ once for a given q , and rescale it as needed for any source/lens redshift combination. With circular symmetry broken, we would not necessarily expect the doubly limited cross sections for the various image pairings to be of the form (8), but our numerical calculations show that such a form in fact yields a very good approximation. The solid curves in Figures 1 and 2 show $\sigma(\mu_{\min})$ and $\sigma(\Delta t_{\max})$ for the three independent quad image pairings of least time delay for an SIE lens model with axis ratio $q = 0.65$. $\sigma(\mu_{\min}, \Delta t_{\max})$ can then be constructed for each image pairing as per (8). For a given q , $\sigma(\mu_{\min}, \Delta t_{\max})$ of any quad image pairing is limited by the full angular area of the region in the source plane enclosed by the tangential caustic. This area increases as the lens becomes more elliptical, and is approximately $0.095 \theta_E^2$ for $q = 0.65$ as seen in Figures 1 and 2.

By comparing the solid SIE curves of Figures 1 and 2 to the dotted SIS double-imaging curve, we see that the introduction of ellipticity significantly increases the cross section for multiple-image lensing with relatively short time delays as compared to the circularly symmetric SIS-lens case, at the cost of reduced fainter-image magnification¹. Of the three independent image pairings in the quad case, the 2nd/3rd image pairing is most significant for affording both large magnification and short time delay; these are the two images that will merge and annihilate if the source crosses outside the tangential caustic. When the source approaches the center of the lens, the four images form a cross and the 2nd/3rd image time delay approaches its maximum value. This limit can be found by solving the lens equation in closed form for the special case of a source directly behind the lens center:

$$\Delta t_{\max, 2 \text{ to } 3} = \frac{\tau}{2(q^{-1} - q)} \left(\operatorname{arctanh}^2 \sqrt{1 - q^2} - \arctan^2 \sqrt{q^{-2} - 1} \right) . \quad (10)$$

For $q = 0.65$, this is about 0.14τ as seen in Figures 1 and 2. For a lens redshift $z_L < \sim 0.1$, the lensing timescale τ as defined in (6) will be $< \sim 25 h_{70}^{-1}$ years for a cluster velocity dispersion $\sigma_v = 1000$ km/s, and all 2nd/3rd image pairings of a $q = 0.65$ lens will have time delays of less than $\sim 3.5 h_{70}^{-1}$ years. Thus although sources very near to the caustic will indeed have very short time delays as shown by Kovner & Paczyński (1988), sources *anywhere* within the tangential caustic can still be lensed into multiple images with observationally acceptable

¹Here we are comparing the high-magnification behavior of a circular lens to that of an elliptical lens. For any *particular* elliptical lens, a quad configuration will be of greater total magnification than a double, since the quadruple-imaging cross section carves out the very highly magnified region of the source plane directly behind the lens. Hence observed quad-image QSO lenses generally have greater magnification than doubles.

time delays. Furthermore, as the 2nd/3rd image time delay approaches its maximum, the 1st/2nd and 3rd/4th image time delays approach zero for reasons of symmetry, so (10) is in fact only an upper limit on the shortest time delay experienced by any quadruply imaged source.

With all other parameters fixed, both τ and θ_E^2 scale as the fourth power of the cluster velocity dispersion σ_v . Therefore if the axes of Figure 2 were labeled in units of years and square arcseconds (instead of in units of τ and θ_E^2), an increase in σ_v would rescale both axes by the same factor. This fact together with the differing concavities of the curves shown in Figure 2 indicates that in delay-limited cases, increasing σ_v will increase an SIE-quad cross section, but decrease an SIS-double cross section.

3.3. Nonsingular Isothermal Ellipsoid

A singular isothermal core is perhaps an unrealistic feature to assume in a galaxy cluster. To investigate sub-isothermal core behavior, we can add a core of angular radius s to the SIE to obtain the nonsingular isothermal ellipsoid (NIE):

$$\kappa = \frac{1}{2} \frac{b}{\sqrt{s^2 + q\theta_x^2 + q^{-1}\theta_y^2}} . \quad (11)$$

To compare the lensing behavior of models with differing core radii, we must take care to adopt a sensible normalization. In the limit $s \rightarrow 0$, b may be identified with θ_E from above, but to compare singular and nonsingular models the normalization $b = \theta_E$ is inappropriate. Instead we take

$$b = \frac{\theta_E}{\bar{\theta}_E} \left(sq + \sqrt{s^2 + \bar{\theta}_E^2} \right) , \quad (12)$$

where $\bar{\theta}_E$ is the Einstein radius (5) evaluated for a source at some fiducial redshift \bar{z}_S . With this normalization, κ retains the proper scaling with changing source redshift, and the tangential critical curve crosses the major axis of the lens at fixed position $\bar{\theta}_E/\sqrt{q}$ with varying s for a source at redshift \bar{z}_S . This choice is meant to respect (approximately) the constraint that would be placed on the cluster mass distribution by a giant arc at redshift \bar{z}_S .

Several changes occur when we increase the core radius from zero. First, the model now has two angular scales, b and s . For a given lensing cluster, b will change with varying source redshift while s remains fixed. The scale invariance of the lens is broken, and the lensing behavior changes qualitatively between source planes at different redshifts; we now need to compute cross sections for a range of s/b and to scale them appropriately. Second, in

multiple-imaging configurations, an additional image that was previously infinitely demagnified in the singular core becomes in principle observable (accordingly, the “radial cut” of the singular case is now the “radial caustic”). This new image corresponds to a maximum of the arrival-time function (1). In this study we exclude these “maximum” images from consideration so as to have continuity of the total cross section $\sigma(\mu_{\min}, \Delta t_{\max})$ from the singular case when summing the contributions of all independent image pairings. (Actual core images could also get lost in the light of a cluster cD galaxy.) Finally, although the overall cross section for multiple imaging decreases with increasing core radius through a contraction of the radial caustic, the area enclosed by the *tangential* caustic actually *increases* slightly. The decreased curvature of the arrival-time surface in the central regions of the lens also leads to larger magnifications and shorter time delays. Thus the cross section $\sigma(\mu_{\min}, \Delta t_{\max})$ at fixed μ_{\min} , Δt_{\max} tends to increase for all image pairings as the core radius is increased, until the formation of naked cusps begins to reduce the cross section for the 3rd/4th image pairing. The dashed lines in Figures 1 and 2 show the cross sections for the same image pairings as in the SIE case above, but for an NIE lens at the so-called “umbilic catastrophe” and for sources at the same redshift as the normalization redshift \bar{z}_s . Here the umbilic catastrophe refers to the particular s value at which the expanding tangential caustic completely engulfs the shrinking radial caustic; see Kassiola & Kovner (1993) Figure 1(c) for an illustration. The NIE cross sections for the 1st/2nd and 2nd/3rd image pairings are increased over the SIE case at all values of μ_{\min} , Δt_{\max} . All 2nd/3rd image pairings now have time delays $<\sim 0.06\tau$.

3.4. More Complicated Models

The detailed lensing behavior of a real galaxy cluster cannot be captured entirely by the models considered above. The effects of unmodeled cluster substructure are likely to be somewhat similar to the effects of increasing cluster ellipticity relative to the circular case: higher image multiplicity, shorter time delays between multiple images, and reduced magnification. In fact, ellipticity may be thought of as the leading order of substructure beyond circular symmetry. By considering the perhaps exaggerated axis ratio $q = 0.65$ we hope to approximate unmodeled substructure effects. An obvious refinement would be to carry out our cross section calculations using a more detailed and realistic cluster mass map, but we defer this possibility to future investigations. Our primary goal is to estimate the detection rates of multiply imaged SNe in a single cluster field that would be useful for the determination of H_0 , and thus we confine our attention to the preceding models.

4. Accuracy of H_0 Determination

First we will examine the usefulness of a measured time delay in determining H_0 within the simplified context of the SIE lens model. By the convenient result published by Witt, Mao, & Keeton (2000) for self-similar isothermal lenses, the time delay between images A and B is given by

$$\Delta t_{AB} = \frac{1}{2c} \frac{D_L D_S}{D_{LS}} (1 + z_L) \left(|\vec{\theta}_B|^2 - |\vec{\theta}_A|^2 \right) , \quad (13)$$

with the image positions measured relative to the lens center. cH_0^{-1} factors out of the D 's on the right-hand side. The dependence on the cosmological parameters (Ω_M, Ω_Λ) is generally weak but worth noting. For example, taking a lens redshift of 0.1 (0.3) and a source redshift of 1, $D_L D_S / D_{LS}$ changes only by about 1% (3%) as Ω_Λ goes from 0 to 0.7 in flat universes. (If we allow for unknown cosmological density parameters, then our time delay will not give us H_0 , but rather the distance measure $D_L D_S / D_{LS}$.) Assuming the image positions, source and lens redshifts, and time delay can be measured with high accuracy, the greatest source of error in an H_0 determination is due to the uncertainty $\delta\vec{\theta}_0$ in the position of the center of the lens. From (13), this is

$$\frac{\delta H_0}{H_0} = 2 \frac{(\vec{\theta}_B - \vec{\theta}_A) \cdot \delta\vec{\theta}_0}{|\vec{\theta}_B|^2 - |\vec{\theta}_A|^2} \equiv \vec{V} \cdot \delta\vec{\theta}_0 / \theta_E . \quad (14)$$

For positions of 2nd/3rd image pairings obtained numerically, the dimensionless vector \vec{V} ranges in magnitude from 2 for source positions near the lens center to almost zero for source positions just inside the tangential caustic. \vec{V} is approximately of unit magnitude for source positions of area-weighted median fainter-image magnification. The fractional error in an H_0 determination is then roughly equal to the uncertainty (parallel to the image separation vector) of the lens center position in units of the Einstein angular scale θ_E defined in (5) and evaluated for the source redshift of the SN. However, the magnification of both images increases as the source approaches the tangential caustic, so a magnification bias favors the detection of events with smaller fractional uncertainties in the derived H_0 .

Of course, our real hope would be to use not an SIE model (nor even an NIE model) but a detailed lens model that takes full account of lensing constraints like giant arcs and multiply imaged galaxies. In this more general case, the fractional uncertainty in a derived H_0 value will be related to the fractional uncertainty in the lensing potential $\psi(\vec{\theta})$ and the square of its gradient, evaluated at the two SN image positions. (This can be seen by substituting (2) into (1) to eliminate the source position $\vec{\beta}$.) Based on their nonparametric lensing inversions, AbdelSalam et al. (1998a,b) report fractional uncertainties in the convergence κ of $\leq 20\text{--}25\%$ in the strong lensing regions of interest in the clusters Abell 370 (using 6

multiple-image systems) and Abell 2218 (using 3 multiple-imaged systems and a number of singly imaged, distorted arclets). They demonstrate clearly that the mass distribution becomes more tightly constrained as the number of nearby lensed images increases. The dramatic increase in multiply imaged sources that ACS and later instruments can uncover should certainly push the uncertainty in reconstructed cluster mass distributions well below 10% in the inner cluster regions. Furthermore, strong-lensing features constrain the potential directly, and the potential is an integral over the mass distribution. Hence we expect the uncertainty in the cluster potential (the more relevant uncertainty for H_0 determination) to be less than the uncertainty in the reconstructed mass distribution. SN image positions (and perhaps flux ratios, if microlensing and differential extinction effects are negligible) also provide local constraints on the potential, further improving the accuracy of a time-delay H_0 value. Taken together these considerations suggest that statistical H_0 errors on the order of a few percent should be attainable if successful observations can be made. And as noted in the introduction, the lens model will not be subject to systematic errors associated with a global mass sheet degeneracy as long as multiple-image constraints are available for sources at different redshifts.

To estimate the error that could arise due to time-delay contributions from unmodeled galaxy-scale substructure, we note that time delays scale as the square of the characteristic deflection of the lens, which in turn scales as the square of the lens velocity dispersion, as in (5) and (6). With a time delay of $0.1\tau_{\text{cluster}}$, a cluster velocity dispersion of 1000 km/s, and a perturbing galaxy velocity dispersion of 200 km/s, the induced fractional error in H_0 would be

$$\frac{\delta H_0}{H_0} = \frac{\tau_{\text{galaxy}}}{0.1\tau_{\text{cluster}}} = \frac{(200)^4}{0.1 \times (1000)^4} = 1.6\% . \quad (15)$$

Thus substructure is unlikely to be a source of large error in the determination of H_0 from an observed time delay. An appreciable substructure perturbation to the overall cluster potential would also affect lensed SN image positions (which can themselves constrain the potential), so it could not go entirely unmodeled by a reconstruction that makes use of all lensing constraints.

5. Predicted Detection Rates

We wish to quantify detection rates for observable SN image pairings with acceptably short time delays. Since type II (core-collapse) SNe will be detected with much higher frequency than type Ia's (Sullivan et al. 2000, for example), we focus exclusively on the former. Assuming a Salpeter IMF with lower and upper mass cutoffs of $0.1 M_\odot$ and $125 M_\odot$ respectively, and that all stars with mass above $8 M_\odot$ result in core-collapse SNe, Madau (1998)

derives a conversion factor of 0.0074 between solar masses of star formation and eventual number of type II SNe. The comoving star formation rate density at a given redshift can in turn be related to an observable quantity such as comoving rest-frame ultraviolet luminosity density, which is seen to rise sharply out to the redshifts of $z \sim 1$ that we would hope to probe in our search (Madau, Pozzetti, & Dickinson 1998).

Here we consider two versions of the cosmic star formation rate density as a function of redshift. First, following Sullivan et al. (2000, “SFH-I”), we use the form of Madau & Pozzetti (2000) corrected to a lower mass cutoff of $0.1 M_{\odot}$ and adjusted from an Einstein-DeSitter (EdS) universe to our assumed Λ CDM cosmology in the manner described by Hogg (2001). This form incorporates an upward correction to account for extinction (Madau 2000; Madau & Pozzetti 2000). We also consider the greatest and least of the three star formation rate density functions reported by Lanzetta et al. (2002) based on their determination of the star formation rate intensity distribution function from redshifts $z = 0$ –10, again converted from EdS to Λ CDM. These authors do not attempt an extinction correction, and we work directly with their “unobscured” star formation rate densities.

We can combine our assumed SN rate densities with multiple-imaging cross sections $\sigma(\mu_{\min}, \Delta t_{\max})$ computed numerically for the SIE and NIE in an integral over source redshifts to obtain an estimate of the detection rates that we might expect:

$$\begin{pmatrix} \text{SN image pairings} \\ \text{per cluster} \\ \text{per obs. year} \end{pmatrix} = \int_{z_L}^{\infty} \frac{1}{1+z} \dot{\rho}_{\text{SN}}(z) \sigma(\mu_{\min}, \Delta t_{\max}) \frac{dV_C}{d\Omega dz}(z) dz . \quad (16)$$

$dV_C/d\Omega dz$ is the comoving volume per unit solid angle per unit redshift, the angular cross section depends upon source redshift and includes a contribution from each independent image pairing, $\dot{\rho}_{\text{SN}}(z)$ is the rate density of core-collapse SNe per unit comoving volume per unit proper time, and the factor of $(1+z)^{-1}$ converts from proper time at the source to observer time. In an actual calculation this integral must be cut off at some upper limit beyond which the supernova rate density becomes utterly unknown.

To obtain a numerical estimate, we assume a $\sigma_v = 1000$ km/s lensing cluster at redshift $z_L = 0.2$ with an isodensity axis ratio $q = 0.65$ (as mentioned above, with the exaggerated ellipticity we hope to approximate the effects of cluster substructure). We take the maximum tolerable observer-frame time delay between multiple images to be $3 h_{70}^{-1}$ years, and investigate a range of differences between limiting detectable apparent magnitude m_{lim} and SN II absolute magnitude M_{SN} . We model the SN II spectrum as that of a 10,000-K blackbody (Filippenko 1997), and compute AB-magnitude k -corrections for observations at 8140 Å (I -band). We consider both an SIE model and an NIE model with a core radius of $30h_{70}^{-1}$ kpc (subtending about 9.1 arcseconds). We normalize the NIE model for $\bar{z}_S = 0.7$

as described in Section 3.3, taking this as a typical giant-arc redshift from Williams et al. (1999). Figure 3 shows the result of a detection-rate integration out to a redshift of $z = 8$. For visual clarity, we do not plot the NIE rates for the two Lanzetta et al. (2002) star-formation histories; they show the same increase by a factor of ~ 2 over the singular case as do the Madau & Pozzetti (2000) NIE rates. The results shown are relatively insensitive to the choice of upper integration limit, since the star formation rate density of Madau & Pozzetti (2000) drops steeply at high redshift, and the k -correction imposes an effective cut-off on any contribution from the enhanced high- z star formation reported by Lanzetta et al. (2002).

Although we have considered type II SNe as our sources, a rough idea of the detection rates for type Ia SNe image pairings can be obtained from Figure 3 by assuming that type Ia's are ~ 10 times less frequent and ~ 1 magnitude brighter than type II's. Under these assumptions, detection rates for type Ia events are significantly lower than for type II's, and the k -correction appropriate to the intrinsically redder colors of type Ia's will push their rates lower still.

6. Outlook

The estimated detection rates shown in Figure 3 are far in excess of what one would predict based on a circular-cluster lens approximation, and they allow us to gauge the feasibility of a cluster monitor program targeted to detect multiply-imaged SNe for use in determining H_0 . Repeated imaging would be required every month or so, as type II-L (II-P) SNe spend ~ 30 (~ 50) days within one magnitude of maximum light (Doggett & Branch 1985). This time will be stretched by $(1 + z_{\text{SN}})$, but a precise temporal measurement of peak light would be crucial to a time-delay measurement. Taking $m_{\text{lim}} = 24$ and $M_{\text{SN}} = -18$, the most optimistic assumptions predict on the order of 2–3 detectable image pairings per cluster per century. A cluster monitor program operating for two to three years would need to image ~ 50 –100 cluster fields to the required depth in order to have a good chance of detecting a few image pairings. Such a program would be feasible with today's 6–8m-class telescopes with wide-field cameras given several dark nights per month. The project is better suited to a telescope such as the proposed *LSST*, which would operate in a dedicated survey mode, repeatedly imaging large areas of the sky (including strongly lensing clusters) to significant depth. Although our predicted image-pair detection rates are sensitive to assumptions about cluster structure and cosmic star formation history, this method of determining H_0 certainly warrants serious consideration when such observatories as *LSST* become operational, particularly if the current discrepancy between H_0 values from lensing and from other methods remains unresolved.

We stress that in order for this method to be successful, known strong-lensing clusters should be targeted specifically. The best constraints on the cluster potential would ideally be obtained by follow-up observations with instruments such as ACS of clusters for which SN image pairs are actually observed. However, the co-added images from a long-term monitor program would be of significant depth, and could also be searched for strongly lensed background features.

The authors wish to thank Paul Schechter for valuable discussion of these topics, Ian Smail for pointing out the work of Giraud (1992), and the anonymous referee for comments that led to a greatly improved manuscript.

REFERENCES

AbdelSalam, H. M., Saha, P., & Williams, L. L. R. 1998a, MNRAS, 294, 734

AbdelSalam, H. M., Saha, P., & Williams, L. L. R. 1998b, AJ, 116, 1541

Blandford, R., & Narayan, R. 1986, ApJ, 310, 568

Dahlén, T., & Fransson, C. 1999, A&A, 350, 349

Doggett, J. B., & Branch, D. 1985, AJ, 90, 2303

Filippenko, A. V. 1997, ARA&A, 35, 309

Freedman, W. L., et al. 2001, ApJ, 553, 47

Gal-Yam, A., Maoz, D., & Sharon, K. 2002, MNRAS, 332, 37

Giraud, E. 1992, A&A, 259, L49

Gladders, M. D., Yee, H. K. C., & Ellingson, E. 2002, AJ, 123, 1

Goobar, A., Mörtsell, E., Amanullah, R., & Nugent, P. 2002, A&A, 393, 25

Gunnarsson, C., & Goobar, A. 2002, A&A, submitted; also preprint (astro-ph/0211401)

Hogg, D. W. 2001, PASP, submitted; also preprint (astro-ph/0105280)

Holz, D. E. 2001, ApJ, 556, L71

Kassiola, A., & Kovner, I. 1993, ApJ, 417, 450

Keeton, C. R., & Kochanek, C. S. 1998, *ApJ*, 495, 157

Kochanek, C. N. 2002a, *ApJ*, submitted; also preprint (astro-ph/0204043)

Kochanek, C. N. 2002b, *ApJ*, 578, 25

Kochanek, C. N. 2003, *ApJ*, 583, 49

Kolatt, T. S., & Bartelmann, M. 1998, *MNRAS*, 296, 763

Kormann, R., Schneider, P., & Bartelmann, M. 1994, *A&A*, 284, 285

Kovner, I., & Paczyński, B. 1988, *ApJ*, 335, L9

Kneib, J.-P., Mellier, Y., Pelló, R., Miralda-Escudé, J., Le Borgne, J.-F., Böhringer, H., & Picat, J.-P. 1995, *A&A*, 307, 27

Kneib, J.-P., Ellis, R. S., Smail, I., Couch, W. J., & Sharples, R. M. 1996, *ApJ*, 471, 643

Lanzetta, K. M., Yahata, N., Pascarelle, S., Chen, H.-W., & Fernández-Soto, A. 2002, *ApJ*, 570, 492

Linder, E. V., Schneider, P., & Wagoner, R. V. 1998, *ApJ*, 324, 786

Luppino, G. A., Gioia, I. M., Hammer, F., Le Fèvre, O., & Annis, J. A. 1999, *A&AS*, 136, 117

Madau, P. 1998, in *ASP Conf. Ser.* 146, *The Young Universe: Galaxy Formation and Evolution at Intermediate and High Redshift*, ed. S. D'Odorico, A. Fontana, and E. Giallongo (San Francisco: ASP), 289; also preprint (astro-ph/9801005)

Madau, P., Pozzetti, L., & Dickinson, M. 1998, *ApJ*, 498, 106

Madau, P. 2000, *PhST*, 85, 156; also preprint (astro-ph/9902228)

Madau, P., & Pozzetti, L. 2000, *MNRAS*, 312, L9

Marri, S., & Ferrara, A. 1998, *ApJ*, 509, 43

Marri, S., Ferrara, A., & Pozzetti, L. 2000, *MNRAS*, 317, 265

Miralda-Escudé, J., & Rees, M. J. 1997, *ApJ*, 478, L57

Narayan, R., & Bartelmann, M. 1996, preprint (astro-ph/9606001)

Oguri, M., & Kawano, Y. 2003, *MNRAS*, 338, L25

Oguri, M., Suto, Y., & Turner, E. L. 2003, ApJ, 583, 584

Porciani, C., & Madau, P. 2000, ApJ, 532, 679

Refsdal, S. 1964, MNRAS, 128, 307

Saha, P. 2000, AJ, 120, 1654

Saini, T. D., Raychaudhury, S., & Shchekinov, Y. A. 2000, A&A, 363, 349

Schechter, P. L. 2002, in IAU Symp. 201, New Cosmological Data and the Values of the Fundamental Parameters, ed. A. N. Lasenby & A. Wilkinson (San Francisco: ASP), in press; also preprint (astro-ph/0009048)

Schneider, P. 1985, A&A, 143, 413

Schneider, P., Ehlers, J., & Falco, E. E. 1992, Gravitational Lenses (Berlin: Springer-Verlag)

Spergel, D. N., et al. 2003, ApJ, submitted; also preprint (astro-ph/0302209)

Sullivan, M., Ellis, R., Nugent, P., Smail, I., & Madau, P. 2000, MNRAS, 319, 549

Tyson, J. A., & LSST Collaboration 2002, in Proc. SPIE 4836, Survey and Other Telescope Technologies and Discoveries, ed. J. A. Tyson & S. Wolff (Int. Soc. Opt. Eng.), 10; also preprint (astro-ph/0302102)

Williams, L. L. R., Navarro, J. F., & Bartelmann, M. 1999, ApJ, 527, 535

Witt, H. J., Mao, S., & Keeton, C. R. 2000, ApJ, 544, 98

Wu, X.-P., Chiueh, T., Fang, L.-Z., & Xue, Y.-J. 1998, MNRAS, 301, 861

Zaritsky, D., & Gonzalez, A. H. 2003, ApJ, 584, 691

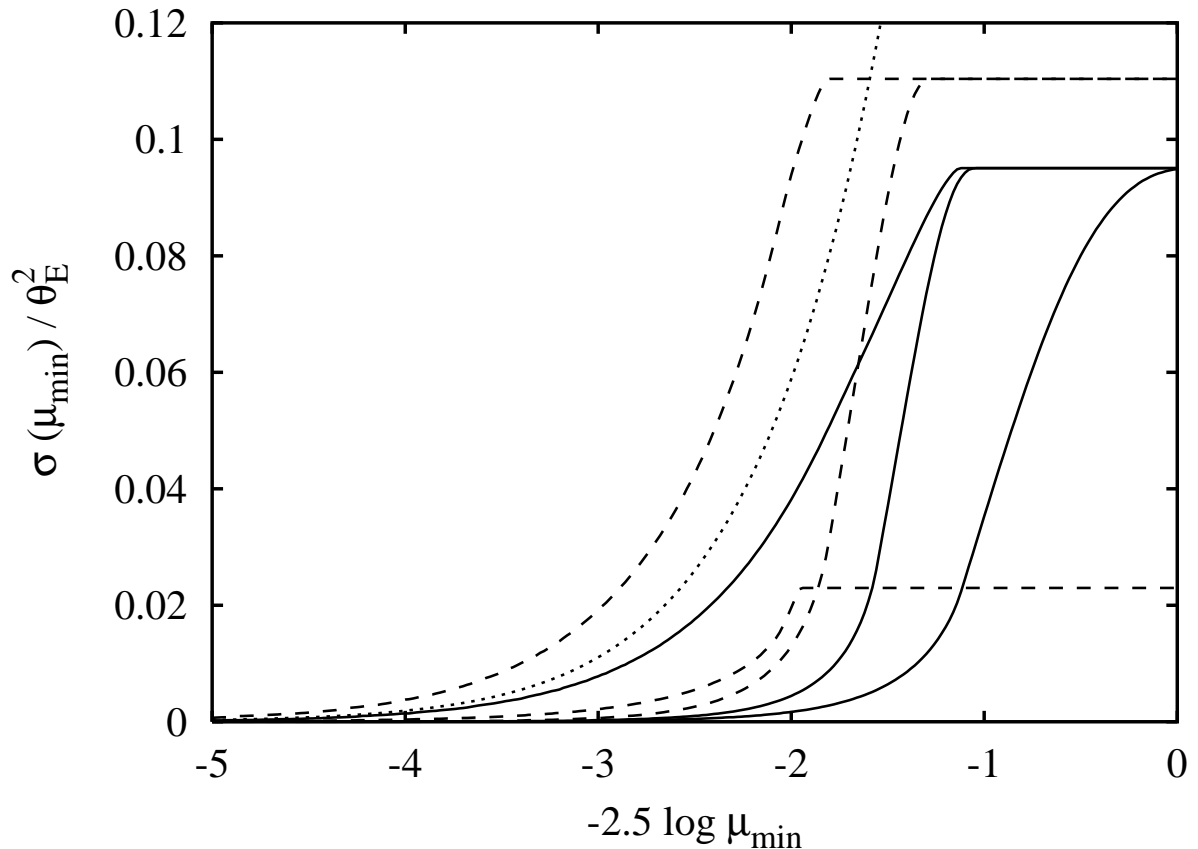


Fig. 1.— Magnification-limited lensing cross sections. Solid lines are for a $q = 0.65$ SIE quad. The upper, middle, and lower curves correspond to the 2nd/3rd, 1st/2nd, and 3rd/4th image pairings respectively. Dashed lines are for the corresponding images of a $q = 0.65$ NIE at the “umbilic catastrophe” and with the normalization $\theta_E = \bar{\theta}_E$ as described in the text. (The curve with the reduced maximum cross section is for the 3rd/4th image pairing.) The dotted curve is for the two images of a $q = 1$ SIS, for comparison.

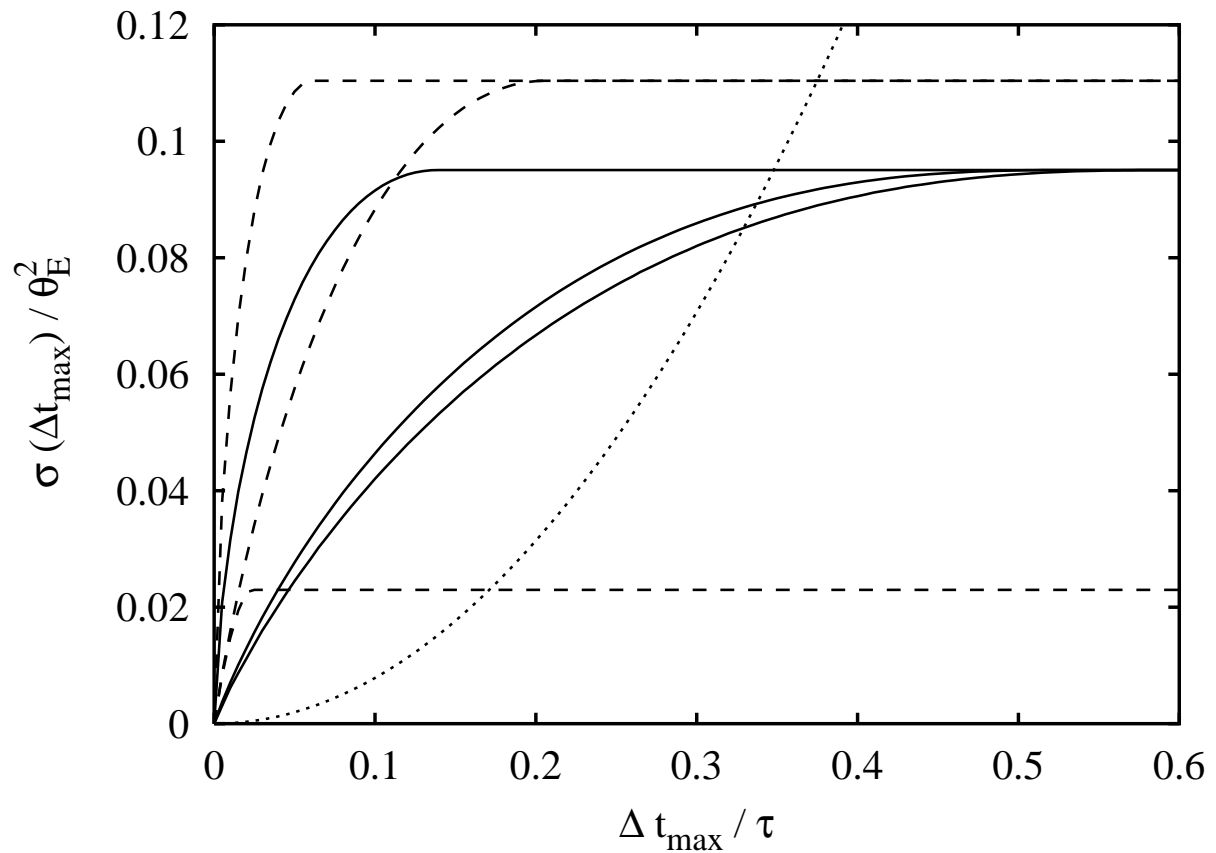


Fig. 2.— Same as Figure 1, but for time-delay-limited lensing cross sections.

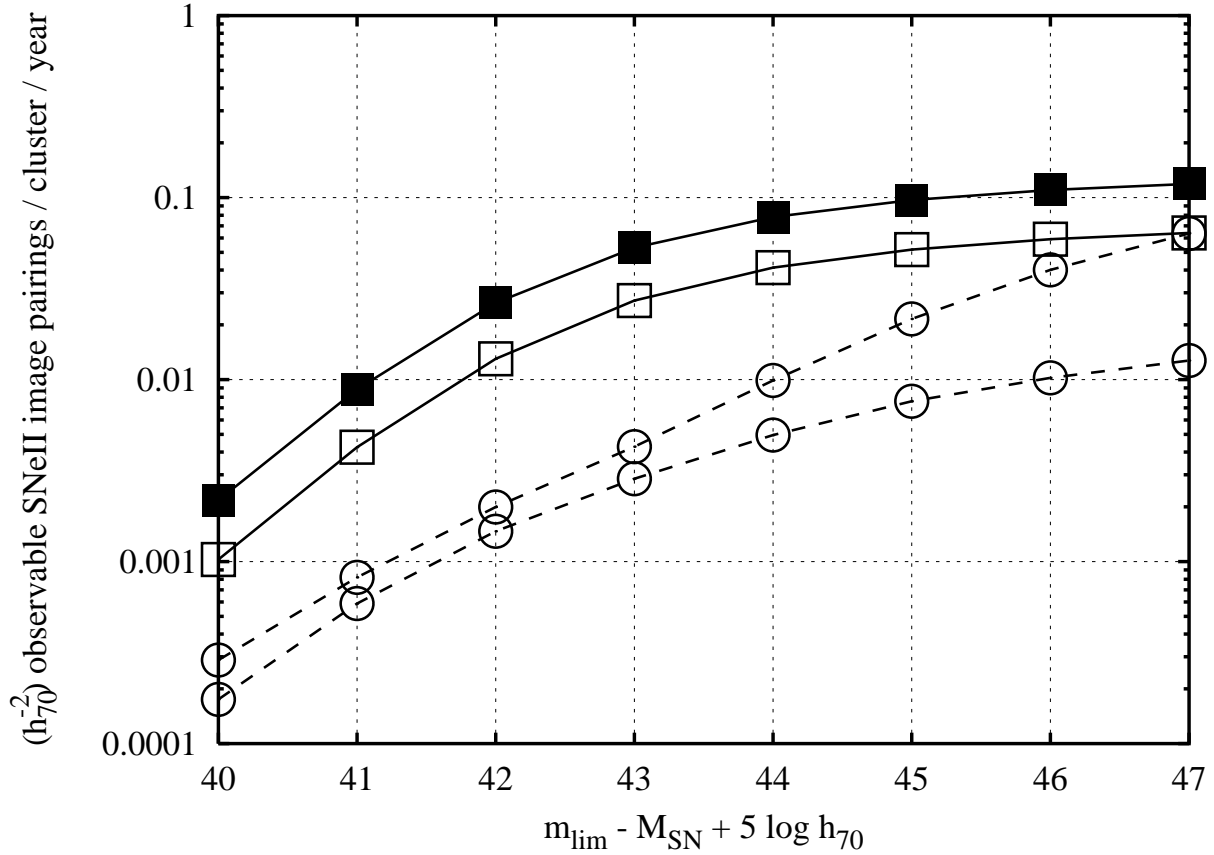


Fig. 3.— Predicted type II SN image pairing detection rates vs. difference between limiting observable magnitude and SN absolute magnitude. (I -band, $\sigma_v = 1000$ km/s, $q = 0.65$, $z_L = 0.2$, maximum observer-frame time delay of $3 h_{70}^{-1}$ years). *Solid lines/squares*: star formation rate density of Madau & Pozzetti (2000). *Dashed lines/circles*: star formation rate density of Lanzetta et al. (2002), upper and lower curves. Open symbols are for an SIE model; solid symbols are for an NIE model with a $30 h_{70}^{-1}$ kpc core radius.